An observational study on the interactions between storm tracks and sea ice in the Southern Hemisphere

Li Zhang[1,2] · Xuya Ren[1,2,3] · Chuan-Yang Wang[1,2] · Bolan Gan[1,2,3] · Lixin Wu[1,2] · Wenju Cai[1,2,4]

Abstract

Using the lagged maximum covariance analysis (MCA), the present study investigates the interannual variability of the storm track in the Southern Hemisphere and the Antarctic sea ice throughout the year. The results show that the two are most tightly coupled in the austral cold seasons. Specifically, storm track anomalies in June and July are associated with a zonal dipole structure of the sea ice concentration (SIC) anomalies in the western Hemisphere, with centers in the Antarctic Peninsula and the Amundsen-Bellingshausen Seas. The storm track can modulate the large-scale atmospheric circulations, which induces anomalous meridional heat transport, downward longwave radiation, and mechanical forcing to further influence the SIC anomalies. The resultant SIC anomalies can last for several months and have the potential to feed back to the storm track. According to the MCA, the influence of the SIC anomalies to the storm track is most evident in August. The SIC dipole along with the SIC anomalies in the Indian Ocean sector have large impact on the storm track activities downstream. The SIC anomalies alters the near-surface temperature gradient and subsequently atmospheric baroclinicity. Further energetic analysis suggests that the enhanced atmospheric baroclinicity facilitates the baroclinic energy conversion from mean available potential energy to eddy available potential energy, and then to eddy kinetic energy, strengthening the storm track activities over the midlatitude Indian Ocean.

Keywords Storm track · Sea ice · Atmospheric circulation · Interannual variability

1 Introduction

Antarctic sea ice has been undergoing rapid and complex changes. From 1979 to 2014, the sea ice extent in the Antarctic region showed an increasing trend (John et al. 2009; Holland 2014) while the global mean surface temperature rose steadily. This is commonly known as the "sea ice paradox". After 2014, the Antarctic sea ice extent experienced a

sharp decreased and since remained at a low level. The sea ice changes are not spatially uniform. Before the sudden sea ice loss, the sea ice trend features a dipole pattern: increasing in the Ross and Weddell Seas and decreasing in the Amundsen-Bellingshausen Seas (ABS) (Ciasto et al. 2015). Studies have shown that these changes of the Antarctic sea ice can be attributed to several factors, including anthropogenic forcing (Thompson and Solomon 2002; Arblaster and Meehl 2006), as well as anomalous atmospheric circulation and oceanic heat flux associated with internal climate variability (Hobbs et al. 2016), e.g., multidecadal variation of the Antarctic–Southern Ocean system (Lecomte et al. 2017; Meehl et al. 2019; Zhang et al. 2019). The Antarctic sea ice also features strong interannual to multi-decadal variability. Many previous studies focus on the atmospheric teleconnections driven by the tropical sea surface temperature (SST) variability (e.g., Yuan 2004; Li et al. 2014; Meehl et al. 2016; Purich and England 2019) while the impact of the mid-latitude ocean and atmosphere variabilities on the Antarctic sea ice have received very little attention.

Li Zhang and Xuya Ren contributed equally to this work.

✉ Chuan-Yang Wang
wangchuanyang@ouc.edu.cn

1   Frontiers Science Center for Deep Ocean Multispheres and Earth System and Key Laboratory of Physical Oceanography, Ocean University of China, Qingdao, China

2   Laoshan Laboratory, Qingdao, China

3   Academy of the Future Ocean, Ocean University of China, Qingdao, China

4   CSIRO Oceans and Atmosphere Flagship, Aspendale, VIC 3195, Australia

The mid-latitude troposphere features prominent synoptic-scale transient eddies, commonly referred to as the storm track from the perspective of wave dynamics (Blackmon et al. 1977). The transient eddies are of great importance for both local and global climate, as they are responsible for almost all the poleward heat transport in the midlatitudes (~90% at 40° S; Trenberth and Caron 2001; Trenberth and Stepaniak 2003). In addition, in the upper troposphere, the meridional transport of the westerly momentum by the storm tracks induces momentum convergence which is crucial for the background atmospheric circulation (Cai and Mak 1990; Branstator 1995). The interaction between the transient eddies and the large-scale background circulations further leads to the low-frequency atmospheric variability at mid and high latitudes (Luo et al. 2011). Hence, the storm track anomalies are also likely to exert impact on the Antarctic sea ice variability. It is difficult to identify the source of the Antarctic sea ice variability in the midlatitudes, due to the low signal-to-noise ratio induced by the large internal variability of the midlatitude atmosphere and the lack of direct sea ice observations (e.g., Overland et al. 2015; Overland et al. 2016). Our recent study attempts to solve this issue by showing that the storm-track activities, induced by the SST anomalies in the South Atlantic, result in hemispheric-scale atmospheric circulation anomalies which modulates the summertime sea ice concentration (SIC) (Zhang et al. 2021). That study only focuses on the austral summer when the oceanic fronts are highly coupled with the atmosphere, while the storm tracks are active in the Southern Hemisphere (SH) throughout the year. Thus, it is still unclear how the sea ice in the polar region respond to the midlatitude forcings in other seasons.

The sea ice variability can feed back onto the midlatitude atmosphere. On the one hand, sea ice anomalies modulate the midlatitude atmosphere by "direct" thermodynamic forcings (Kushnir et al. 2002; Sen Gupta and England 2007). Specifically, large-scale formation of the sea ice can induce substantial surface latent heat release (~100 W m^{-2}) (Alexander et al. 2004). In response to the anomalous diabatic heating, the lower-level atmosphere converges, and the upper-level atmosphere diverges, forming a baroclinic structure in the vertical direction (Li et al. 2023). On the other hand, sea ice variability has the potential to excite transient eddies and modulate large-scale atmospheric circulation via baroclinic processes. The surface air temperature (SAT) across the marginal regions of the sea ice and the open ocean surface shows large horizontal gradient in the meridional direction, much similar to the oceanic frontal zones which has been shown to be important in determining the intensity and location of storm tracks. (Brayshaw et al. 2008; Nakamura et al. 2008; Ogawa et al. 2012).

Some studies based on model experiments attempt to examine the role of the Antarctic sea ice in modulating the midlatitude atmospheric variability. When the sea ice around the Antarctica is artificially removed during the SH cold seasons, the midlatitude jet shows a poleward shift (Simmonds and Budd 1991; Simmonds and Wu 1993; Menéndez et al. 1999). Kidston et al. (2011) further pointed out that the response of the midlatitude jet and storm track to the Antarctic sea ice extent is asymmetric: the jet shift poleward shift when the sea ice extent increases during the cold seasons, but when the sea ice extent decreases, the jet shows no robust responses. During the warm seasons, however, the jet and storm track are not correlated with the extension or contraction of the sea ice edges. Such seasonally asymmetric response of the atmosphere to the sea ice anomalies is due to the seasonal migration of the near-surface baroclinic zone, induced by the thermal contrast between the sea ice and the open ocean, which is located closer to the climatological storm tracks in the cold seasons (Kushnir et al. 2002; Brayshaw et al. 2008). Most previous studies either focus on the long-term variation of the Antarctic sea ice, or use idealized sea-ice perturbation experiments while the observational records suggest that the Antarctic sea ice shows strong interannual variabilities with uneven spatial distribution (Li et al. 2021), complicating our understanding on sea ice-storm tracks interactions in the SH.

The present study investigates the relationship between the SH storm track activities and the Antarctic sea ice variability on the interannual timescales. As the storm tracks are zonally symmetric and active throughout the year in the SH midlatitudes (Nakamura and Shimpo 2004; Zhang et al. 2018), we use lagged maximum covariance analysis (MCA) to examine the seasonal evolution of the coupled variability between the storm track anomalies and the SIC anomalies in the SH. The rest of the paper is organized as follows. Section 2 introduces the data and the lagged MCA methods to extract the storm track and sea ice anomalies. Section 3 investigates the impact of the storm track activities on the Antarctic sea ice. Section 4 focuses on the feedback of the sea ice anomalies to the storm track. Section 5 is the summary with discussions.

2 Data and methods

We use daily atmospheric data on a 0.25°×0.25° grid for the period of 1979–2020 provided by ERA5 reanalysis data from European Center for Medium Range Weather Forecasts (ECMWF; https://www.ecmwf.int/en/forecasts/datasets/reanalysis-datasets/era5). SIC is also provided by ECMWF, which is from the Ocean and Sea Ice Satellite Application Facility (OSISAF) dataset. This SIC is independent from, but consistent with SIC obtained from National Snow and Ice Data Center (NSIDC). Anomalies are obtained by subtracting the monthly climatology, and then the long-term trends and low-frequency variability are removed based on a third-order polynomial. The ENSO influence is removed

based on a linear regression approach (Zhang et al. 2018; Ren et al. 2022).

The lagged MCA is applied using the monthly averaged of the SH storm tracks and Antarctic SIC to find the leading mode with the maximum covariance between the two fields in each month. Here, the storm tracks are defined as the 2–8-day band-pass filtered meridional eddy heat flux at 850 hPa ($\langle v'T' \rangle$). The $\langle \cdot \rangle$ denotes monthly average, and v' and T' denotes the meridional wind and temperature anomalies on the synoptic scale (2–8-day band-pass filtered), respectively. There are mainly two reasons for us to choose $\langle v'T' \rangle$ to represent the storm-track: (1) it is important in transporting the westerly momentum downward to maintain a low-level westerly jet; and (2) its anomaly is closely related to the anomalous surface temperature and surface heat flux at the air–sea boundary. The storm track activity can also be measured by the $\langle v'v' \rangle$ at 250 hPa, and we have found the choice of the measurement does not change the major conclusion of the present study (not shown). The confidence level of the lagged MCA is measured by a Monte-Carlo test with the squared covariance (SC) and squared covariance fraction (SCF). In the test, MCAs are computed with the original Antarctic SIC anomalies and 100 temporally randomly permuted storm tracks, and the probability distribution function of the 100 SCs/SCFs is then constructed to determine the confidence level for the actual statistic.

3 Impact of the storm track activities on the Antarctic sea ice variability

We start by analyzing the relationship between the storm tracks and the Antarctic sea ice. The lagged MCA has been applied between the storm track activities ($\langle v'T' \rangle$) at 850 hPa in the SH midlatitudes (30°–60° S) and the SIC anomalies over the Antarctic regions in all calendar months. The SC and SCF for the first MCA mode show maxima for sea ice in July and August with the storm track leading by 1 month (Fig. 1), suggesting the potential role of the storm track in modulating the Antarctic sea ice variability in austral winter. The sea ice in September and October also shows high covariance with the storm track when the latter leads by 2 and 3 months, respectively. The temporal evolution of the SC and SCF reveals the prolonged influence of the storm track activities in June and July on the Antarctic sea ice variability. SC and SCF are also significant between the SIC in August and storm track in September, indicating possible feedbacks of the sea ice to the storm track activity in austral early spring.

To evaluate the impact of the storm track activities on the sea ice, the spatial distributions of the lagged MCAs between the 850 hPa $\langle v'T' \rangle$ and the Antarctic SIC are shown in Fig. 2. The homogenous (left panel) and heterogenous (right panel) maps are obtained by regressing the $\langle v'T' \rangle$ time coefficient $\langle v'T' \rangle$ of the first MCA mode onto
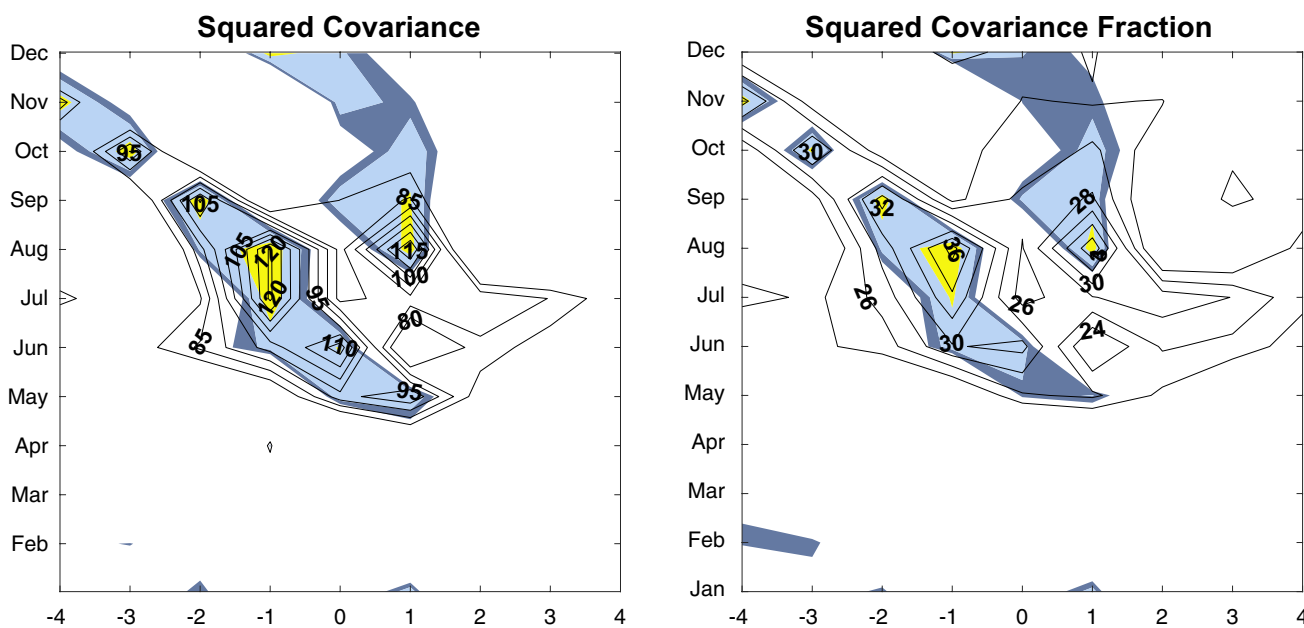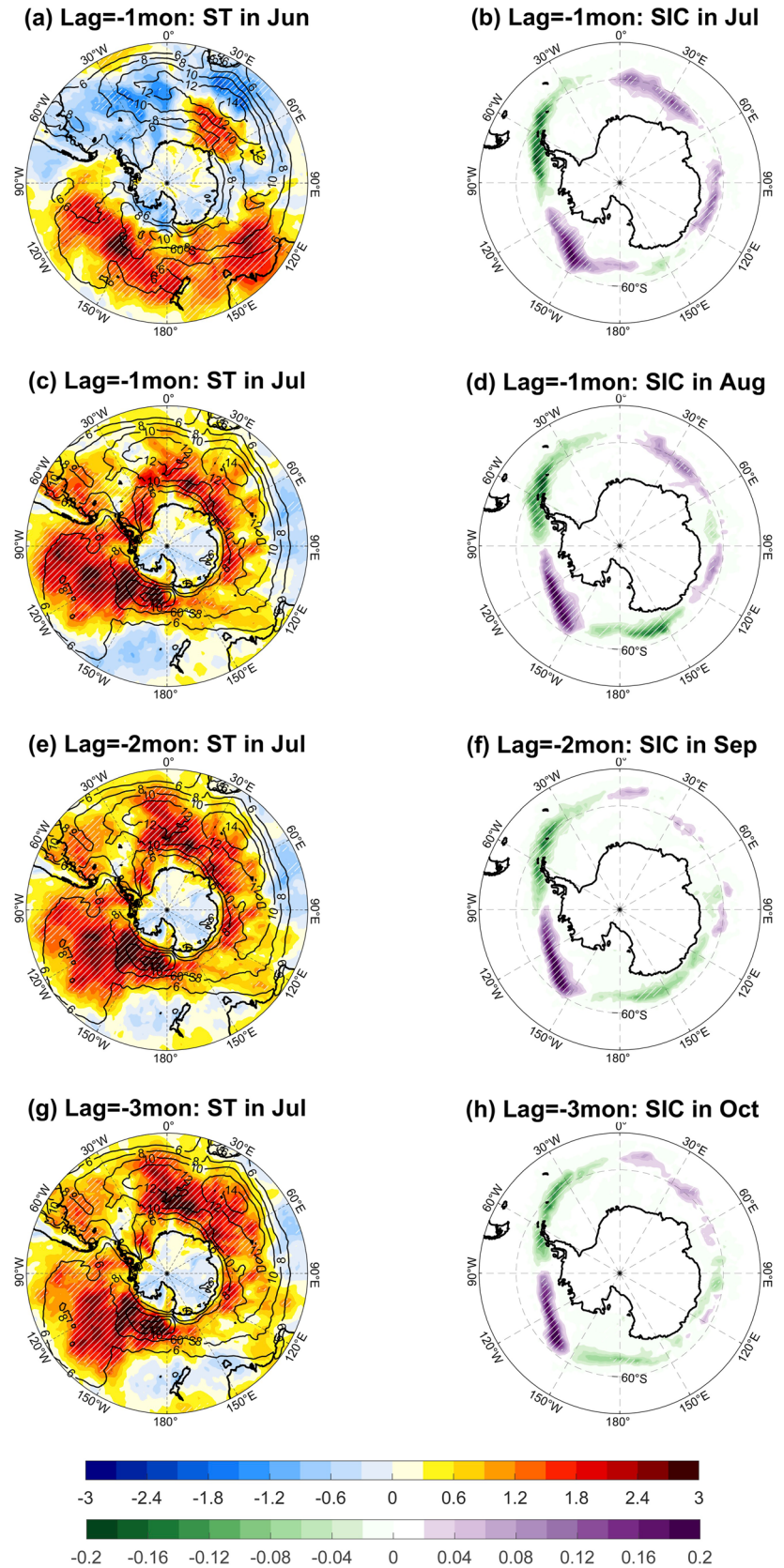

Fig. 1 SC (10^3) and SCF (10^{-2}) of the first MCA mode between SIC and storm tracks represented by (left) 850 hPa $\langle v'T' \rangle$ in the SH midlatitudes. SCs are dimensionless as SST and storm-track fields have been normalized. Shading indicates statistical significance at the 85% (dark blue), 90% (light blue), and 95% (yellow) confidence level based on the Monte Carlo test. Ordinate is the calendar month of SIC, and abscissa is the time lag in month, with positive (negative) for SIC (storm tracks) leading storm tracks (SIC)

Fig. 2 Homogeneous maps for **a** 850 hPa $\langle v'T' \rangle$ (K m s^{-1}) in June and heterogeneous maps for **b** SIC (%) in July corresponding to the first MCA mode at lag − 1 month, derived from the regression against the normalized time coefficients of $\langle v'T' \rangle$ in June. In **c–h**, homogeneous maps for storm tracks (K m s^{-1}) and heterogeneous maps for SIC (%) corresponding to the first MCA modes with storm tracks fixed in **c/e/g** July and SIC lagging by **d/f/h** 1/2/3 months. Contour in **a/c/e/g** denotes storm tracks climatology. Hatching denotes regressions significant at the 95% confidence level

(a) Lag=-1mon: ST in Jun

(b) Lag=-1mon: SIC in Jul

(c) Lag=-1mon: ST in Jul

(d) Lag=-1mon: SIC in Aug

(e) Lag=-2mon: ST in Jul

(f) Lag=-2mon: SIC in Sep

(g) Lag=-3mon: ST in Jul

(h) Lag=-3mon: SIC in Oct

the SH $\langle v'T' \rangle$ and the SIC anomalies, respectively. The storm track activities for the leading MCA modes show distinct patterns in June and July. In June, positive $\langle v'T' \rangle$ anomalies cover the majority of the midlatitude ocean from the south of Australia (~110° E) to the west coast of the South America (~90° W), enhancing the climatological storm track (Fig. 2a). In most parts of the Atlantic and Indian Ocean sectors, on the other hand, the $\langle v'T' \rangle$ shows relatively weak negative anomalies in the midlatitudes, except for the region over 30°–60° E, where the $\langle v'T' \rangle$ shows a meridional dipole, shifting the background storm track southward (Fig. 2a). In July, on the other hand, the anomalous $\langle v'T' \rangle$ is positive across the entire SH midlatitudes, greatly enhancing the background storm track across all longitudes (Fig. 2c, e, g). Specifically, over the Atlantic and Indian Ocean sectors, the anomalous $\langle v'T' \rangle$ peak at ~60° S, south of the climatological storm track, while over the Pacific sector, the anomalies are generally in phase with the climatological distribution of the storm track.

The SIC anomalies, on the other hand, show a robust zonal dipolar pattern in the western Hemisphere (Fig. 2b, d, f, h) in all months analyzed. Negative SIC anomalies are centered around the Antarctic Peninsula (AP), and positive anomalies are located around 90°–150° W in the Pacific sector. SIC anomalies are relatively weak in the eastern Hemisphere and show some seasonal variation. Specifically, positive SIC anomalies can be found in the Indian Ocean sector (0°–60° E) and southwest of Australia (80°–120° E) in July and August, with the storm track leading by 1 month in June and July, respectively (Fig. 2b, d). In August to October, the SIC, associated with $\langle v'T' \rangle$ anomalies in July, shows negative anomalies in the eastern part of the Pacific sector (120° E–180°) (Fig. 2f, h). Because of the transient nature of the storm track variability and the distinct spatial distributions in June and July, we focus on two pairs of storm track-SIC relationships in the following analysis, namely storm track in June versus SIC in July and storm track in July versus SIC in August. Figure S1 shows the normalized time coefficients of the storm track (SIC) anomalies in June and July (July and August) obtained by the respective first MCA modes. The two SIC indices are highly correlated with the storm track indices with a lag of 1 month. All four indices shown here display strong interannual variability, with prominent periods of 4–5 years.

A natural question arises as to why the distinct $\langle v'T' \rangle$ anomalies in June and July can induce similar SIC responses in the Antarctic region. It has been documented that the storm track activity and SIC are dynamically linked by the modulated large-scale circulations such as the background westerly jet (e.g., Zhang et al. 2021). Figure 3 shows the spatial distribution of the zonal wind anomalies in July and August associated with the respective $\langle v'T' \rangle$ anomalies in

1 month prior. As expected, the westerlies in response to the anomalous storm track activities show equivalent barotropical structures in both months, with negative anomalies in the lower latitudes and positive anomalies in the midlatitude and subpolar regions. In July, the anomalous westerlies induced by the June $\langle v'T' \rangle$ anomalies feature an annular pattern encircling the Antarctic in both upper and lower troposphere (Fig. 3a, c). Because the background westerly jet shows different spatial distributions in the upper and lower levels, the barotropic zonal wind responses have different climate effects at 200 hPa and 850 hPa. At 200 hPa, the zonal wind anomalies induced by the $\langle v'T' \rangle$ intensifies the jet on its poleward flank in the South Indian Ocean and eastern South Pacific while weakens the jet in the Atlantic sector. Over the western Pacific, the westerly anomalies induced by the storms are located near the exit region of subpolar jet, while the negative anomalies in the lower latitudes weaken the subtropical jet. At 850 hPa, due to orographic blocking, the climatological jets are located over the Southern Oceans and further to the pole compared to the upper levels, the anomalous westerlies then act to enhances the background westerlies. The zonal wind anomalies in August (associated with the $\langle v'T' \rangle$ anomalies in July) are largely similar over the eastern part of the South Pacific and Indian Ocean compared to the anomalies in July in both upper and lower levels. Over the western to mid Pacific, on the other hand, the anomalous westerlies induced in July are replaced with easterlies, weakening the background subtropical jet at the upper level while the anomalies weaken in the Atlantic sector. Despite the discrepancies in the midlatitudes, the zonal wind anomalies in the subpolar region are largely comparable in July and August.

The eddy-induced zonal wind anomalies are diagnosed by the divergence of the horizontal Eliassen–Palm (EP) flux $(\nabla \cdot \boldsymbol{E})$ (Trenberth 1986). The horizontal EP flux can be written as $\boldsymbol{E} = (u'^2 - v'^2/2, -u'v')$, where u' and v' denote the 2–8-day band-pass-filtered zonal and meridional wind anomalies, respectively (Zhang et al. 2018). The zonally averaged EP flux divergence $\nabla \cdot \boldsymbol{E}$ at 200 hPa is shown in Fig. 4 for both July and August associated with the $\langle v'T' \rangle$ anomalies at lag − 1. The $\nabla \cdot \boldsymbol{E}$ induced by storm track activities shows positive anomalies at 42°–70° S (52°–68° S) and negative anomalies at 25°–42° S (40°–52° S) in July (August), both acting to enhance the climatological divergence on its poleward flank and weaken it on the equatorward flank. The anomalous $\nabla \cdot \boldsymbol{E}$ then enhances and weakens the westerlies in subpolar and subtropical respectively, consistent with the spatial distribution of the zonal wind anomalies (Fig. 3; Zhang et al. 2018). The results here suggest that the storm track activities can drive the large-scale atmospheric response through an eddy–mean flow interaction, and thus may influence the Antarctic sea ice.
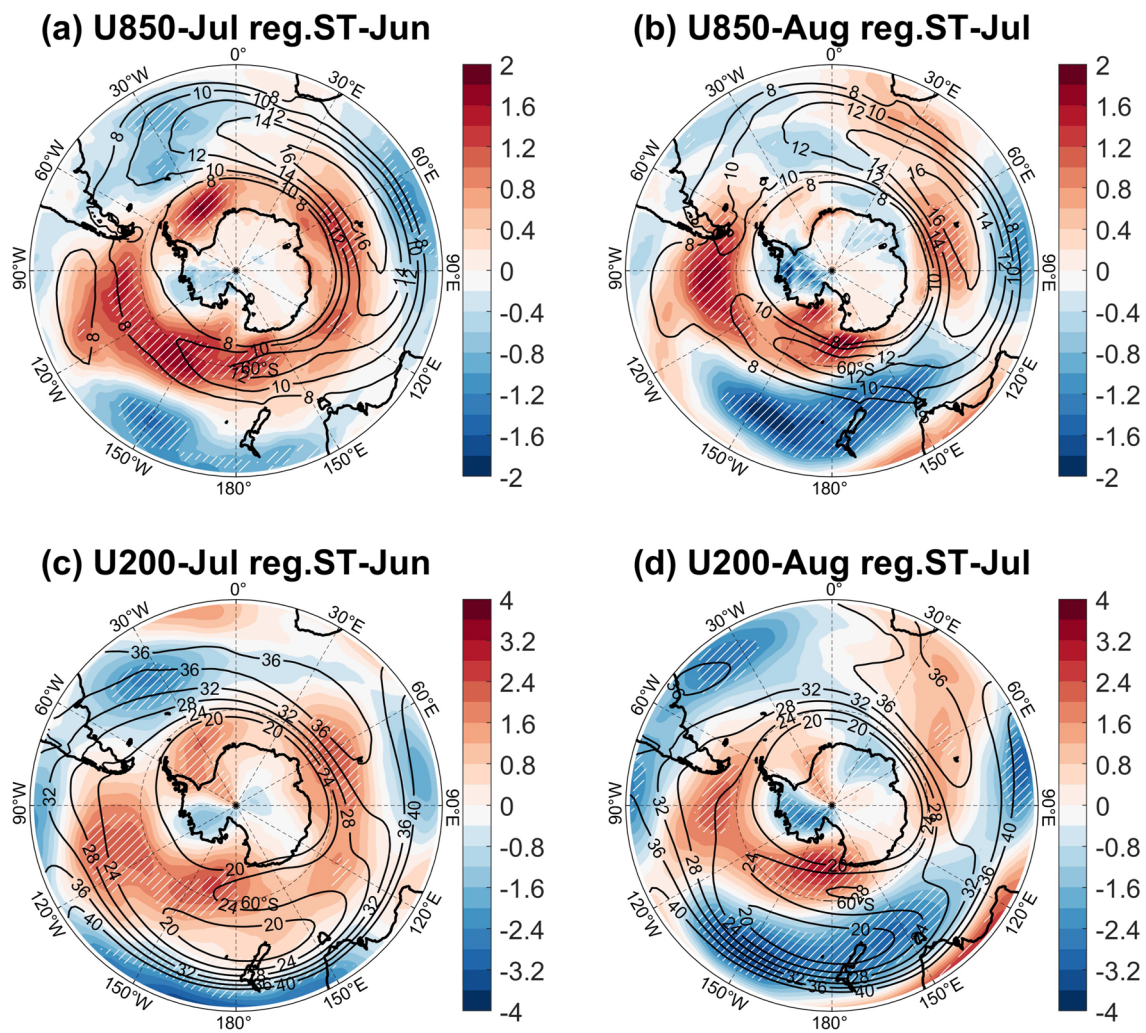
(a) U850-Jul reg.ST-Jun

(b) U850-Aug reg.ST-Jul

(c) U200-Jul reg.ST-Jun

(d) U200-Aug reg.ST-Jul

Fig. 3 Lagged regression of **a** 850 hPa and **c** 200 hPa zonal wind (m s^{-1}) in July against the $\langle v'T' \rangle$ time coefficients in June at lag −1 month, along with the corresponding climatology (contours). **b**, **d** As in **a**, **c**, but for the zonal wind in August and $\langle v'T' \rangle$ in July. Hatching denotes regressions significant at the 95% confidence level

Figure 5 shows the geopotential height anomalies in July and August associated with the $\langle v'T' \rangle$ time coefficients in 1 month prior. The geopotential height anomalies in both months show apparent barotropic structure, with positive centers over the southeastern Pacific, Weddell Sea, and central South Indian Ocean, and negative centers over the ABS. Such barotropic structure indicates that the geopotential height anomalies are likely induced by the synoptic eddy activities (e.g., Fang and Yang 2016; Gan et al. 2022). Note that the storm tracks and large-scale atmospheric circulation can be mutually affected (e.g., Francis et al. 2019, 2020). To isolate the forcing of the storm tracks, we then diagnose the eddy-induced geopotential height tendency using geopotential height tendency equation (Nishii et al. 2009; Gan et al. 2022):

$$\frac{\partial \overline{Z}}{\partial t} = \left[\nabla^2 + f^2 \frac{\partial}{\partial p} \left(\frac{1}{\sigma} \frac{\partial}{\partial p} \right) \right]^{-1} \times \left\{ -\frac{f}{g} \nabla \cdot \overline{\mathbf{V}_h' \zeta'} + \frac{f^2}{g} \frac{\partial}{\partial p} \left[\frac{\nabla \cdot \overline{\mathbf{V}_h' \theta'}}{-(\partial \Theta / \partial p)} \right] \right\}$$

where $\sigma = -\alpha \Theta^{-1} (\partial \Theta / \partial p)$ is the background static stability parameter, α is the specific volume, ζ is the relative vorticity, Θ is the potential temperature of the background state, prime denotes synoptic-scale (2–8 days) fluctuations, and overbar denotes monthly mean. The geopotential height tendency $\partial \overline{Z} / \partial t$ is associated with the transient eddy vorticity (first term on the RHS, denoted as $\overline{Q_{eddy}}$) and the transient eddy heating forcing (second term on the RHS, denoted as $\overline{F_{eddy}}$). $\overline{Q_{eddy}}$ and $\overline{F_{eddy}}$ represents the convergence of vorticity flux and heat flux transport by transient eddies, respectively. Convergence (divergence) of the eddy vorticity flux corresponds to positive (negative) $\overline{Q_{eddy}}$ anomaly, and $\overline{F_{eddy}}$ is

Fig. 4 Lagged regression of **a** 200 hPa $\nabla \cdot E$ ($\times 10^{-2}$ m^2 s^{-2} km^{-1}) in July against the $\langle v'T' \rangle$ time coefficients in June at lag -1 month, zonally averaged over the SH (0°–360° E) for the regressed anomalies (blue line) along with the corresponding climatology (red line). **b** As in **a** but for the 200 hPa $\nabla \cdot E$ in August and $\langle v'T' \rangle$ in July. Hatching denotes regressions significant at the 95% confidence level
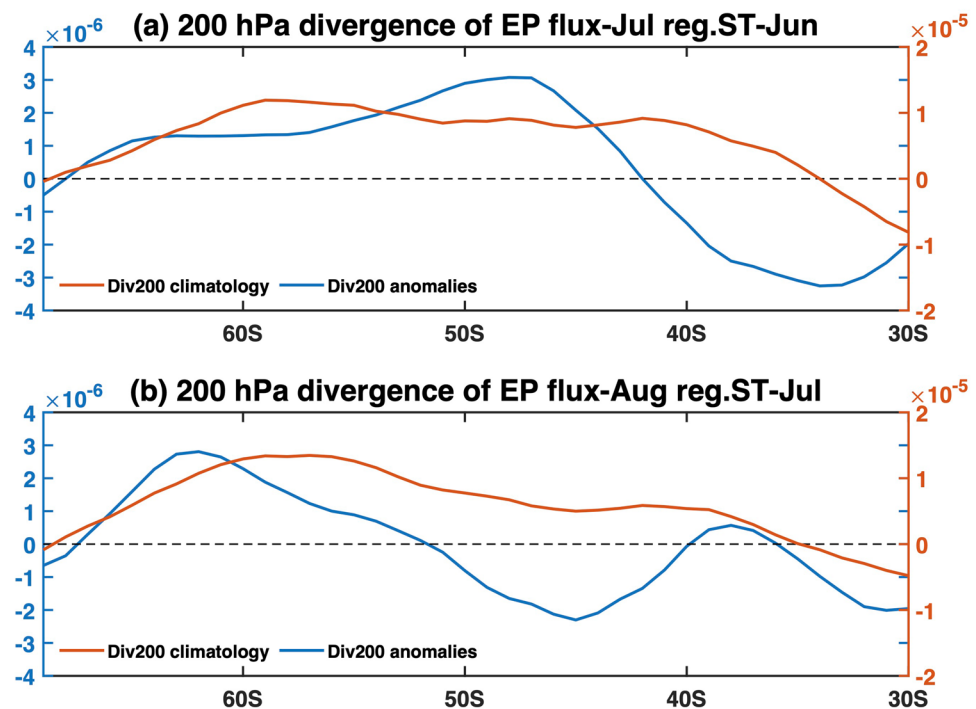
proportional to the vertical gradient of the heating within a certain region. Therefore, the atmospheric transient eddy activities can influence the monthly mean atmospheric circulation by transporting both heat and vorticity fluxes.

The spatial distribution of the computed eddy-driven $\partial \overline{Z}/\partial t$ are generally consistent with the geopotential height anomalies obtained by the lagged MCA, especially on the lower levels (Figs. 6 and 7). $\overline{Q_{eddy}}$ shows a clear barotropic structure and determines the spatial distribution of the total eddy-driven $\partial \overline{Z}/\partial t$ at all levels. The $\overline{F_{eddy}}$, on the other hand, is somewhat baroclinic in some regions, and has comparable contribution to the $\partial \overline{Z}/\partial t$ at 850 hPa. The total effect acts to modulate the large-scale atmospheric circulation, which can further induce the sea ice anomalies in Antarctica as discussed below.

A previous study (Wu and Zhang 2011) has also shown a close relationship between the SIC and large-scale atmospheric circulation anomalies (geopotential height anomalies at 500 hPa, Z500) throughout the year when the Z500 anomalies leads the SIC by 1 month (Fig. 1 in their paper). This is in sharp contrast with our results between the SIC and storm tracks (Fig. 1), whose relationship is only prominent in June to September. Our results highlight the distinctive role of the storm tracks in modulating the Antarctic sea ice.

The sea level pressure (SLP) anomalies and corresponding thermal–mechanical forcing processes associated with the storm track anomalies leading by 1 month show similar patterns in July and August in the subpolar regions. Negative SLP anomalies are centered over the ABS, accompanied with anomalous low-level cyclonic circulations (Figs. 8a and

9a). The associated anomalous northerlies (southerlies) induce warm (cold) air advection (Figs. 8b and 9b) and onshore (offshore) drifts of the sea ice, contributing to the dipolar patten of SAT (Figs. 8e and 9e) and SIC (Fig. 2b, d) in the western Hemisphere in both July and August, as well as the statistically significant albeit weak positive SAT and negative SIC anomalies over 120° E–180° in August. We note that the above processes are inadequate to explain relative weak positive SIC anomalies in the eastern Hemisphere in July and August (Fig. 2b, d; 0°–60° E, 80°–120° E). As the downward longwave radiation (DLR) induced by water vapor is one of the dominant factors affecting the polar regions (Sato and Simmonds 2021), we investigated the total column water vapor (TCWV), vertically integrated horizontal moisture flux (Q) and DLR associated with the storm track anomalies. Q is written as $Q = \int_0^{P_0} \frac{Uq}{g} dp$, where q is the specific humidity (kg/kg) and U is the horizontal wind; $P_0 = 1000$ hPa and g is the gravitational acceleration. In July, weak negative TCWV (Fig. 8c) anomalies and diverged Q (Fig. 8d) are located in the Indian Ocean sector (0°–60° E) and southwest of Australia (80°–120° E), leading to the decreased DLR (Fig. 8d) and subsequent SAT cooling. This process eventually contributes to the slightly increased SIC therein. Similar processes can also be found in August (Fig. 9c–e) but not as significant. It is also worth mentioning the anomalous DLR also plays a role in contributing to the SIC dipole in western Hemisphere. In addition, the SAT and SIC anomalies are mutually enhanced locally due to the sea ice-albedo-radiation feedbacks.

Z250   Z500   Z850

(a)   (b)   (c)

July

(d)   (e)   (f)

Aug

gpm

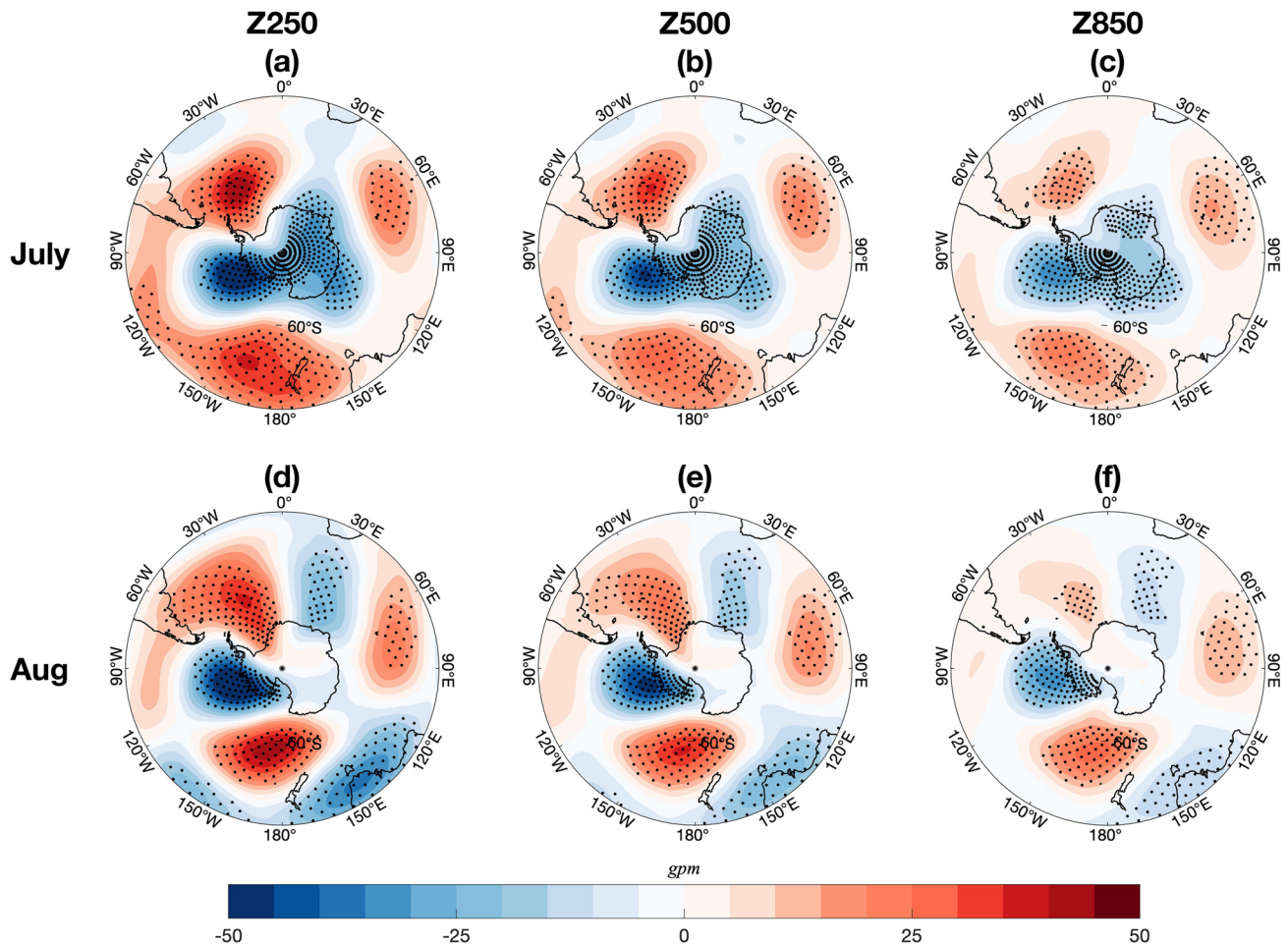-50   -25   0   25   50

Fig. 5 Lagged regression of geopotential height at **a** 250 hPa, **b** 500 hPa and **c** 850 hPa in July against the $\langle v'T' \rangle$ time coefficients in June at lag −1 month. **d–f** As in **a–c**, but for the geopotential height in August and $\langle v'T' \rangle$ in July. Dots denote regressions significant at the 95% confidence level

Eddy transport is the dominant mechanism for the climatological poleward heat and moisture fluxes in the extratropics (Figs. S2a, S3a; Trenberth and Stepaniak 2003; Tsukernik and Lynch 2013). Here we show that the direct eddy transport due to the storm track activities only plays a negligible role in total anomalous heat and moisture transport. We first decompose the vertically integrated meridional moisture flux (MMF) into three components: (1) the first term is associated with the mean meridional circulation (MMC), (2) the second term is from planetary waves or "stationary eddies" (SE), and (3) the third term is from time-varying "transient eddies" (TE). The TE is then further decomposed into the synoptic (2–8 days, TE2–8) and low-frequency (greater than 8 days) components. As shown in Figs. S2 and S3, the anomalous MMF is dominated by the MMC component, which

is one-order-of-magnitude larger than the other terms. In contrast, the TE2–8 is much smaller and features zonally uniform distribution, indicating a weak contribution to the SIC anomalies. Similar results can be found for eddy heat flux (not shown). Overall, we argue that the SIC anomalies are induced by the eddy-driven large-scale atmospheric anomalies rather than the direct eddy heat and moisture transport.

As the reanalysis data are commonly biased for SAT in the Antarctic region, we verify the results using in-situ observation from 40 stations (Fig. 10). Most stations with continuous data records tend to show robust SAT anomalies, especially those in the AP. Specifically, almost all stations show robust positive SAT anomalies in the AP in both July and August, and negative SAT anomalies in the eastern Hemisphere in July. This substantiates our
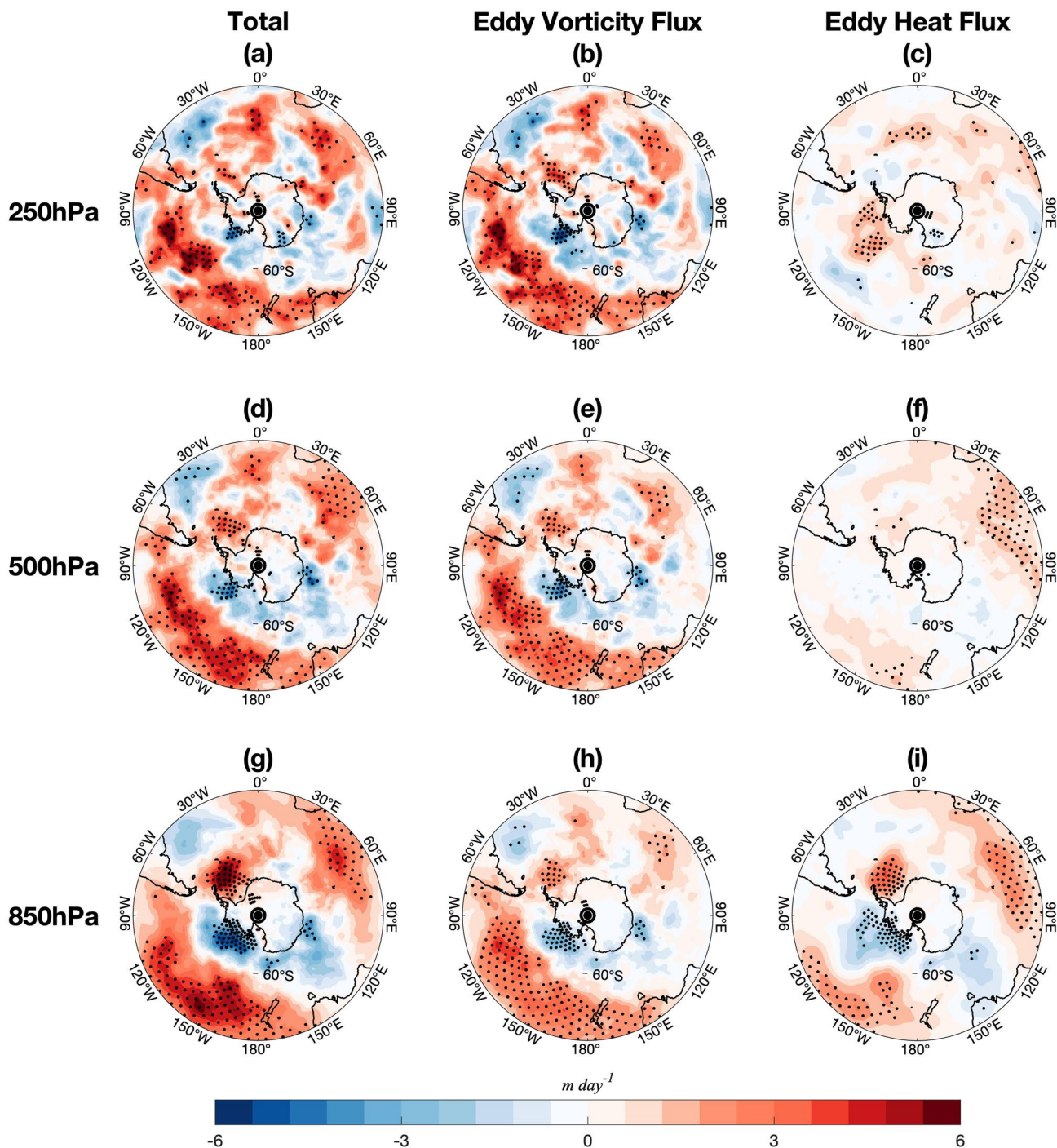
Fig. 6 Regressions on the $\langle v'T' \rangle$ time coefficients in June of Ztend (m day^{-1}) induced by the convergence of (right) transient eddy heat flux, (center) eddy vorticity flux, and (left) the sum of these two fluxes at (top) 250, (middle) 500, and (bottom) 850 hPa in July. Dots denote regressions significant at the 95% confidence level

analysis using the ERA5 reanalysis data. Note that not all station observations pass the 95% confidence level based on the *t*-test, largely due to the discontinued observational records.

4 Feedbacks of the sea ice anomalies to the storm track variability

We have discussed in the previous section that the SIC in August and $\langle v'T' \rangle$ in September show large SC and SCF in the MCA analysis (Fig. 1), suggesting that the sea ice anomalies

Total
(a)

Eddy Vorticity Flux
(b)

Eddy Heat Flux
(c)

250hPa

(d)

(e)

(f)

500hPa

(g)

(h)

(i)

850hPa

$m\ day^{-1}$

-6   -3   0   3   6
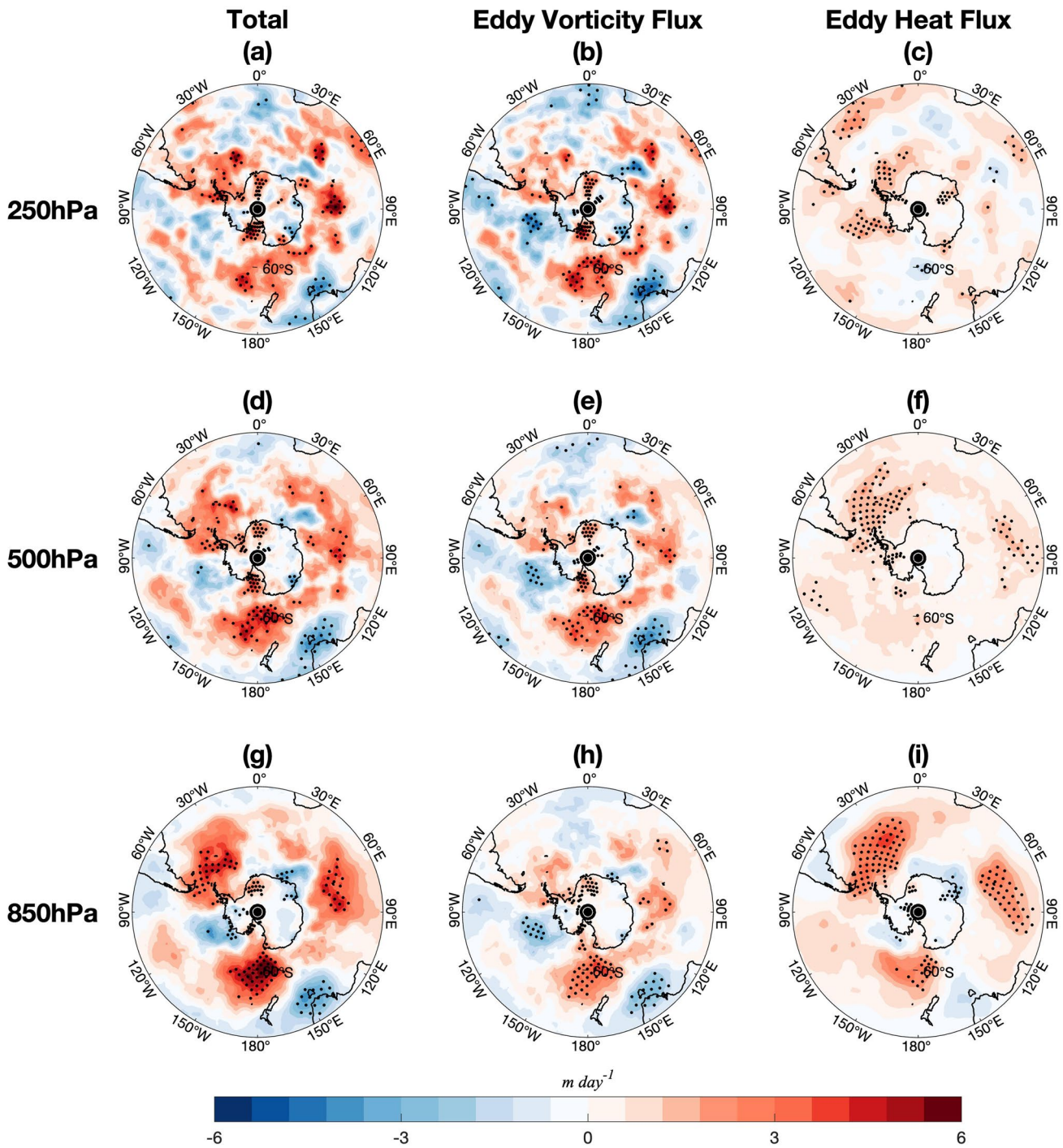
Fig. 7 The same as Fig. 6, but for Ztend in August against the $\langle v'T'\rangle$ time coefficients in July

may have large impact on the storm track activities in austral winter. As the SIC anomalies and the atmosphere are coupled at sub-monthly timescales, we analyze the lag regression of the $\langle v'T'\rangle$ against the SIC anomalies in 1 month prior to isolate the reponse of the storm tracks to the sea ice forcing. Figure 11 shows the homogeneous and heterogenous maps for SIC in August and $\langle v'T'\rangle$ in September, respectively, regressed

against the SIC time coefficient in August. The SIC shows positive anomalies in the ABS, and Indian Ocean and negative anomalies in the vicinity of the AP. The associated positive $\langle v'T'\rangle$ anomalies are mostly concentrated over the Indian Ocean, downstream of the SIC anomaly centers. Interestingly, the SIC distribution shows striking resemblance with the SIC anomalies forced by the anomalous $\langle v'T'\rangle$ variability in July.
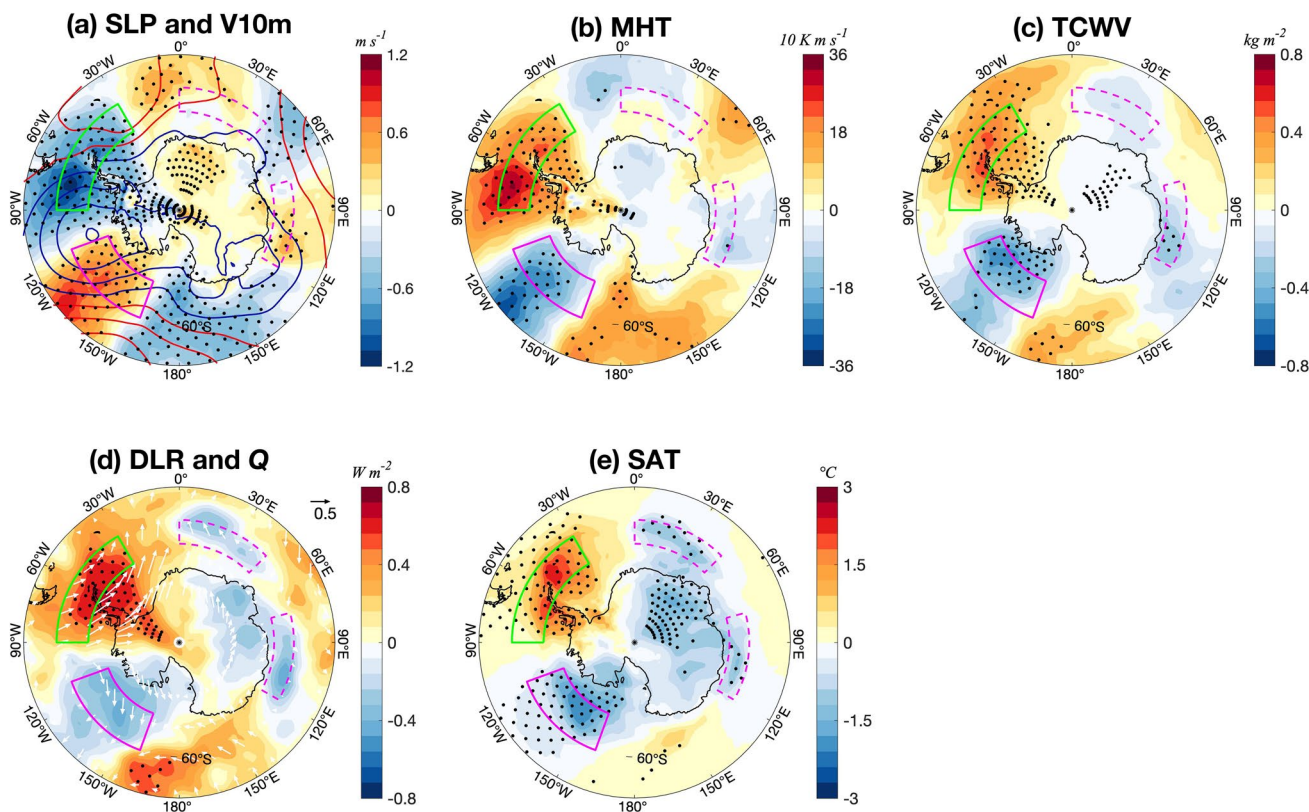
Fig. 8 Lagged regression of **a** SLP (red and blue contours for positive and negative anomalies, respectively at ±100 Pa) and 10 m meridional wind velocity (shadings), **b** poleward vertically integrated meridional heat transport averaged over 1000–850 hPa, **c** total column water vapor, **d** vertically integrated moisture flux (Q; vectors) and downward longwave radiation, and **e** SAT in July against the $\langle v'T' \rangle$ time coefficients in June at lag −1 month. Dots denote regressions significant at the 95% confidence level

This suggests that the SIC anomalies induced by the storm track may feed back to the storm track activities. Furthermore, the time coefficients of August SIC and September $\langle v'T' \rangle$ are highly correlated, and both peak on interannual timescales, at ~4–5 years (Fig. S4).

Preceding studies have pointed out the sea ice anomalies can affect the storm track activities by altering the baroclinicity of the troposphere (e.g., Kidston et al. 2011; Gu et al. 2018). To be specific, the sea ice anomalies induce large temperature gradient over the edges of the sea ice, as the sharp transitional region between the sea ice and the open water features strong horizontal temperature gradient, equivalent to an oceanic front (Nakamura et al. 2008). The anomalous heat and moisture fluxes associated with the sea ice anomalies are likely to modulate atmospheric temperature gradients and subsequently, storm track activities (Zhang et al. 2018; Schemm 2018; Francis et al. 2019, 2020). Here we show the surface heat flux anomalies in September regressed against the SIC time coefficient in August (Fig. 12). The downward latent and sensible heat fluxes are forced by the SIC anomalies, with positive (negative) centers

corresponding to the regions with increased (reduced) SIC. The shortwave radiation anomalies indicate the sea ice-albedo feedback, with opposite signs to the turbulent heat fluxes. The longwave radiation anomalies are relatively weak due to weak moisture anomalies (not shown). Overall, the anomalous turbulent heat fluxes induced by the SIC anomalies may alter the atmospheric baroclinicity and further affect the synoptic eddy activities.

Next, we examine the sea-ice induced atmospheric baroclinity variability by computing the Eady growth rate σ_{Eady} (Eady 1949), defined as $\sigma_{eady} = 0.31g \left(N\overline{\theta} \right)^{-1} \left| \partial\overline{\theta} / \partial y \right|$, where $\overline{\theta}$ is the vertically averaged monthly mean potential temperature between two adjacent pressure levels, and N denotes the Brunt-Väisälä frequency which satisfies $N^2 = -\rho g^2 \overline{\theta}^{-1} (\partial\theta/\partial p)$, and $\rho = PR_d^{-1}\overline{\theta}^{-1}(P_0/P)^{R_d/C_p}$, $P_0 = 1000 \, hP$. The Eady growth rate estimates the maximum growth rate of the most unstable synoptic mode. Contours in Fig. 13 show the climatological σ_{Eady} in August and September. Indeed, the climatological σ_{Eady} peaks over the ocean frontal zones and transitional region between the sea

(a) SLP and V10m

(b) MHT
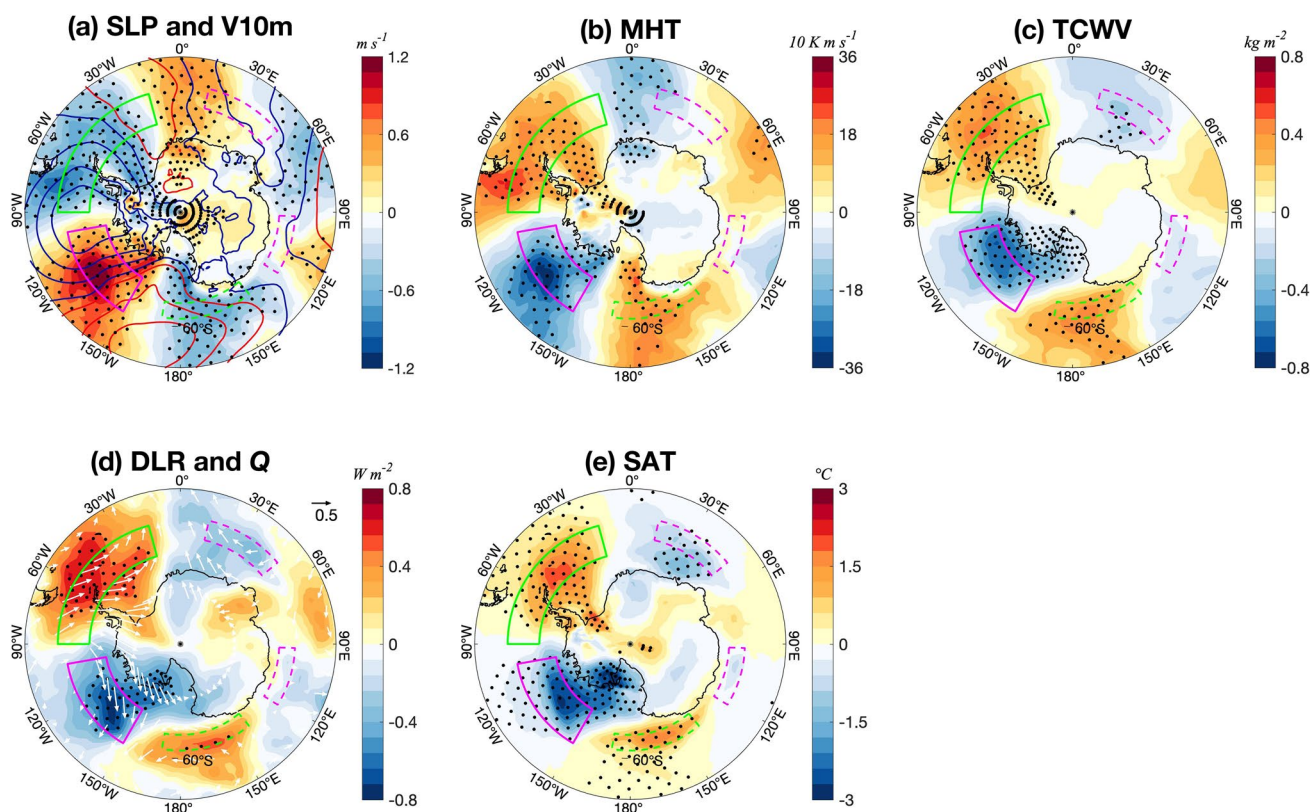
(c) TCWV

(d) DLR and *Q*

(e) SAT

Fig. 9 The same as Fig. 8, but for atmospheric variables in August against the $\langle v'T' \rangle$ time coefficients in July at lag -1 month

ice and open ocean, where the background atmospheric baroclinicity is high.

The σ_{Eady} anomalies in August and September against the time coefficient of the SIC in August obtained by the MCA analysis are also shown in Fig. 13. In the concurrent regression (Fig. 13a), the σ_{Eady} anomalies reflect the direct effect of the sea ice anomalies in modulating the atmospheric baroclinicity. To be specific, the dipole structure of σ_{Eady} anomalies correspond to the locational variation of the sea ice margins associated with the SIC anomalies (Fig. 11a). Take the AP, where the SIC decreases, for example, the edges of the sea ice withdraw to higher latitudes in response to the negative SIC anomalies. This results in a positive σ_{Eady} anomalies on the poleward flank of the SIC anomalies and negative σ_{Eady} anomalies on the equator flank. The opposite applies to the regions with increased SIC. In the following month, the σ_{Eady} anomalies are more zonally uniform compared to August, with two relatively stronger positive centers over the AP and the Indian Ocean sector.

Figure 13b shows the lag regression of the σ_{Eady} in September against the SIC anomalies in September. We have shown in our previous study (Zhang et al. 2018) that the σ_{Eady} can persist for more than 1 month, and the spatial distribution at lag 1 are somewhat different from the concurrent regression. One of the major differences is that the

dipole structure at lag 0 are replaced with relatively zonally uniform positive anomalies at lag 1. Strong positive σ_{Eady} anomalies in September are located at 30°–120° E, which is downstream of the σ_{Eady} dipole in August. Similar downstream development pattern has been detected by Zhang et al. (2020) using CAM5. In a sensitivity experiment where the SST anomalies are perturbed in the South Atlantic, the induced σ_{Eady} anomalies extend to the South Indian Ocean and South Pacific in the following month. The zonally uniform σ_{Eady} anomalies over the SH midlatitudes may be associated with the anomalous eddy heat transport convergence (Zhang et al. 2020).

The anomalous σ_{Eady} provides baroclinic sources for the synoptic eddies, but its impact on the storm tracks is nonlocal. Due to the wave-guide effect of the westerly jet, a series of wave packets generated by the baroclinic sources propagates eastward roughly along the parallels. This is known as the downstream development of the storm track. The SIC anomalies enhance the σ_{Eady} from a zonal-mean perspective (Fig. 13c), which facilitates the developments of the baroclinic wave packets in those latitudes. The propagation of coherent baroclinic wave packets can be illustrated by a longitude-time diagram with the squared eddy meridional wind anomalies for any given month or season and is not sensitive to the year chosen (Lee and
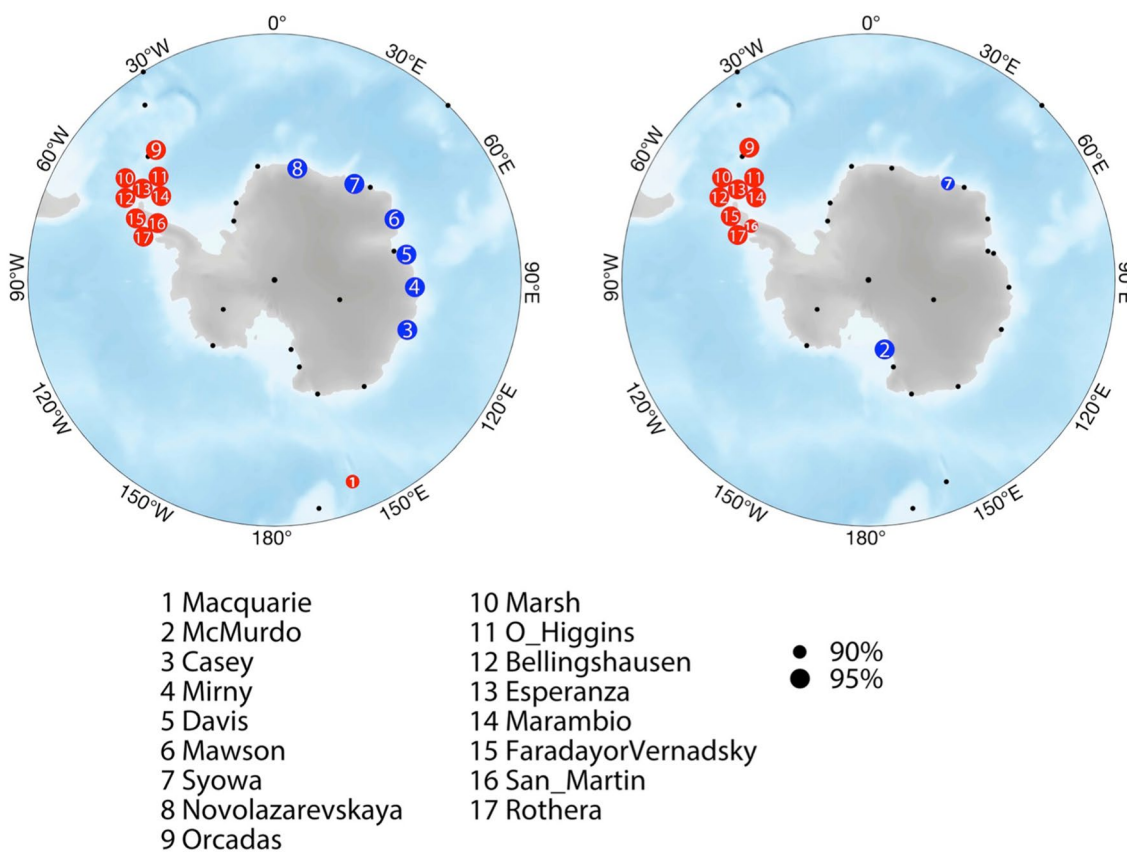
1 Macquarie
2 McMurdo
3 Casey
4 Mirny
5 Davis
6 Mawson
7 Syowa
8 Novolazarevskaya
9 Orcadas

10 Marsh
11 O_Higgins
12 Bellingshausen
13 Esperanza
14 Marambio
15 FaradayorVernadsky
16 San_Martin
17 Rothera

● 90%
● 95%

Fig. 10 (Left) Correlations between SAT observations from 40 stations and $\langle v'T' \rangle$ time coefficients in June at lag -1 month. (Right) The same as (Left), but for $\langle v'T' \rangle$ time coefficients in July at lag -1 month. Circles with red/blue color showing positive/negative correlation, and size corresponding to confidence level
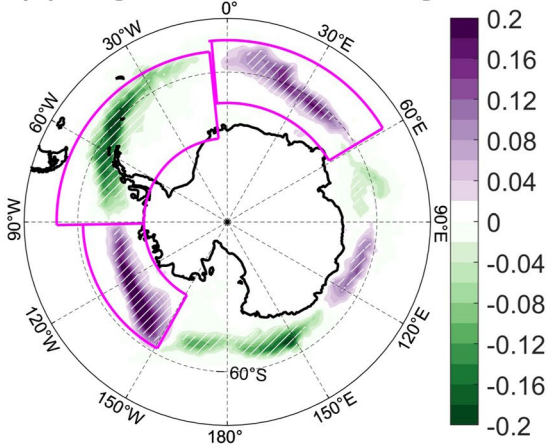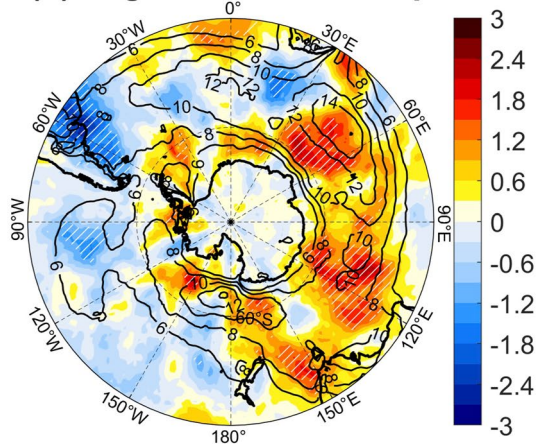
Fig. 11 As in Fig. 2, but for homogeneous maps for **a** SIC (%) in August and heterogeneous maps for **b** 850 hPa $\langle v'T' \rangle$ (K m s^{-1}) in September corresponding to the first MCA mode at lag -1 month, derived from the regression against the normalized time coefficients of storm tracks in September
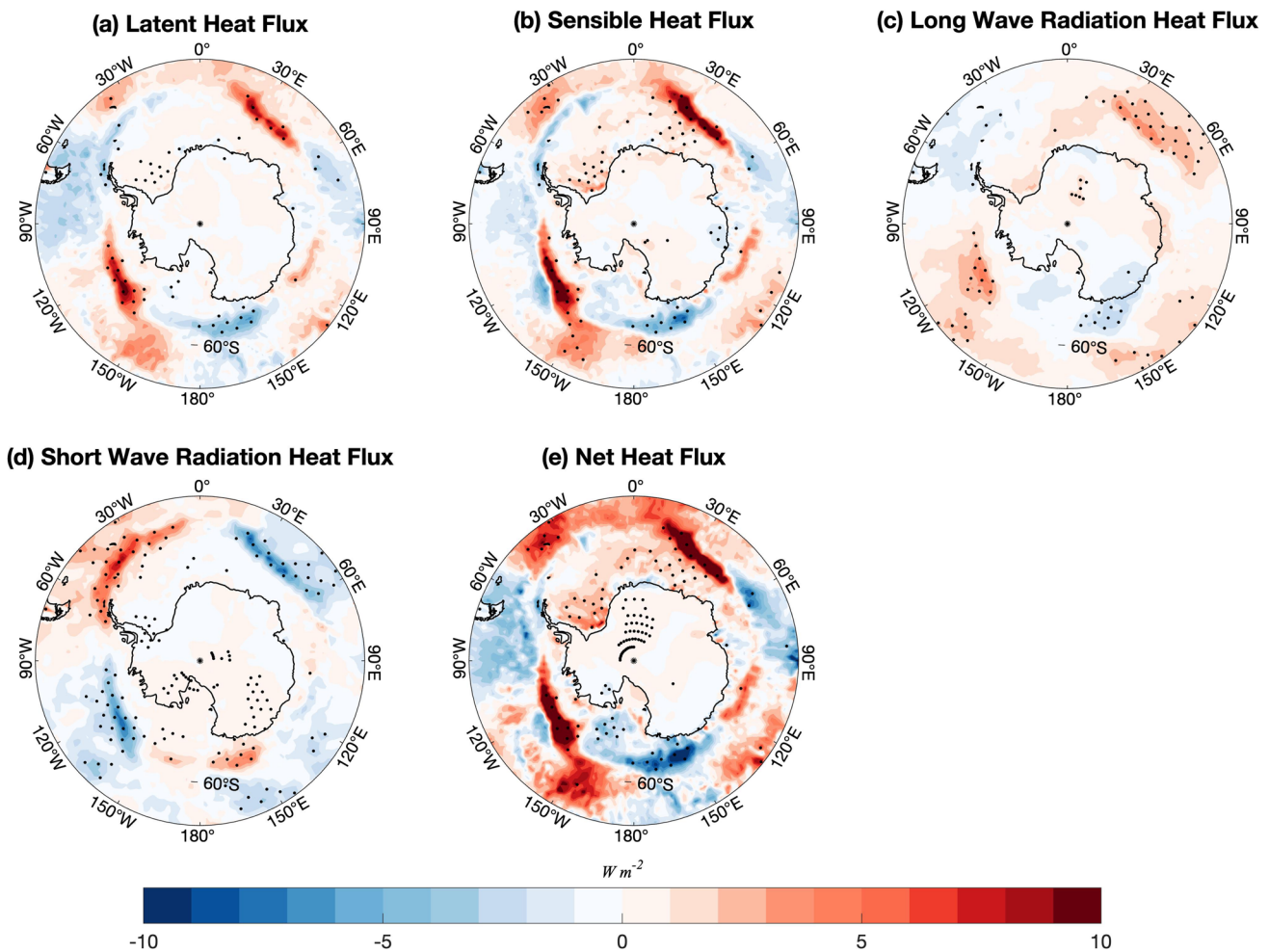
Fig. 12 Lagged regression of **a** latent, **b** sensible, **c** long wave radiation, **d** short wave radiation and **e** net heat flux in September against the SIC time coefficients in August at lag 1 month. Dots denote regressions significant at the 95% confidence level

Held 1993; Zhang et al. 2020). Take Septembers of 1990 and 2010 (Fig. S5a, b) for example, we can clearly see that coherent baroclinic wave packets travelling eastward along the 50° S parallel for one or more circles. Similar patterns can also be observed in other years (not shown). Using a one-point correlation (Fraedrich and Ludz 1987), the estimated group velocity is greater than the phase velocity, indicating downstream development process (Fig. S5c).

To further investigate the effective utilization of baroclinic energy of the mean flow by synoptic eddies, we examine two major baroclinic energy conversion (BCEC) processes (Cai et al. 2007), namely the BCEC from mean available potential energy (MAPE) to eddy available potential energy (EAPE), and from EAPE to eddy kinetic energy (EKE). The BCEC from MAPE to EAPE can be written as $-C_1\left(\frac{P_0}{P}\right)^{R_d/C_p}\left(-\frac{d\theta}{dp}\right)^{-1}\left(\overline{u'T'}\frac{\partial\overline{T}}{\partial x} + \overline{v'T'}\frac{\partial\overline{T}}{\partial y}\right)$ and the BCEC from EAPE to EKE writes as $-C_1\overline{w'T'}$, where $C_1 = \left(P_0/P\right)^{C_v/C_p}R_d/g$. u, v, and w denote the zonal,

meridional wind, and vertical pressure velocity, respectively. Prime ($'$) and overbar denote the 2–8-day band-pass filtered anomalies and monthly average. As shown in Fig. 14, the anomalous SIC tends to enhance the energy conversion from MAPE to EAPE over the midlatitude Indian Ocean and extends downstream to the eastern Pacific, where the climatological MAPE to EAPE is high. The conversion from EAPE to EKE shows similar distribution. From the energetic analysis, we can clearly see that the anomalous sea ice in August can alter the baroclinicity of the mid-latitude atmosphere, facilitating the energy conversion from MAPE to EAPE and then to EKE, enhancing the storm track activities ($\langle v'T'\rangle$) in the Indian Ocean sector (Fig. 14b).

The spatial distribution of the baroclinic energy conversion (BCEC) does not always collocate with the source of baroclinicity (i.e., σ_{Eady}), especially in the Southern Hemisphere (e.g. Zhang et al. 2018, 2020). The travelling wave packets tends to gain energy at certain location along its journey, usually at the regions with high climatological
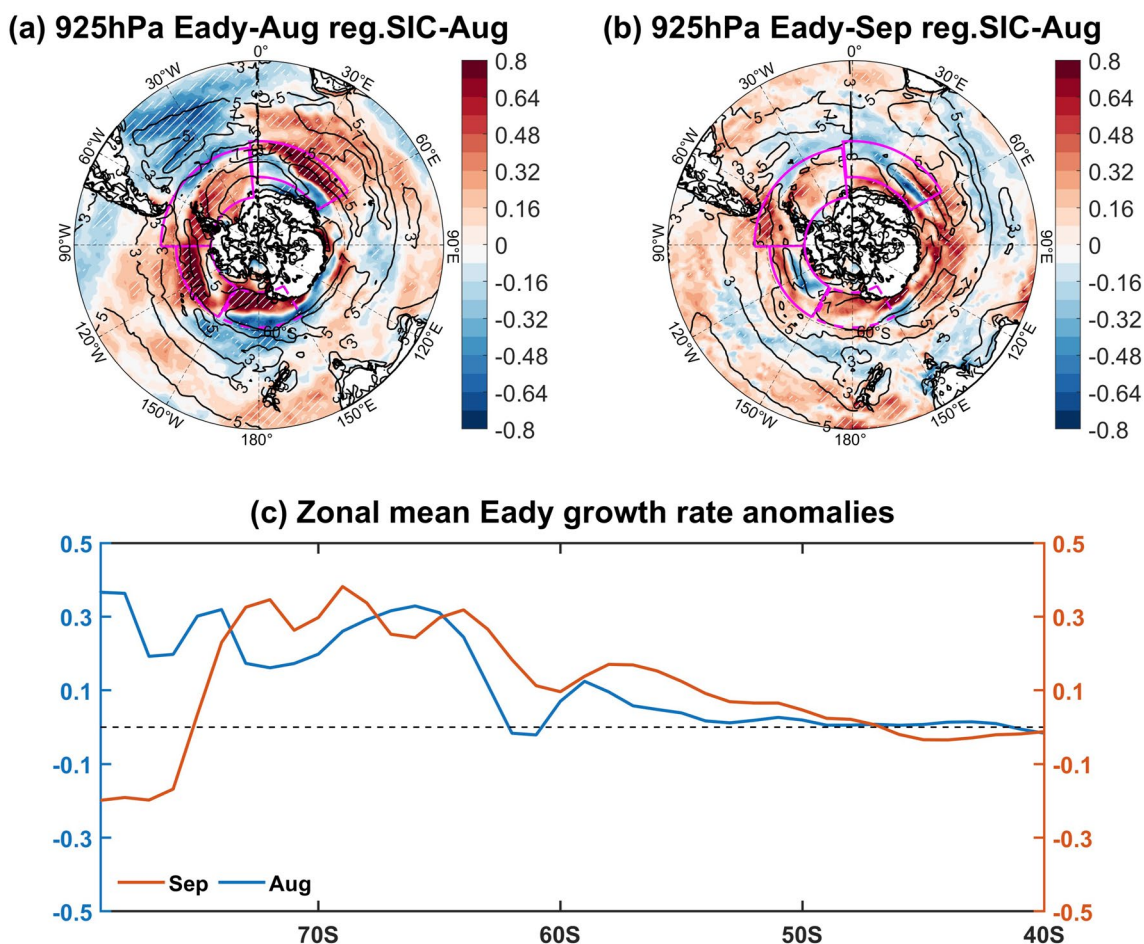
Fig. 13 Lagged regression of 925 hPa Eady growth rate ($\times 10^{-2}$ day^{-1}) in **a** August and **b** September against the SIC time coefficients in August at lag 1 month, along with the corresponding climatology (contours). Hatching denotes regressions significant at the 95% confidence level. **c** Zonally averaged for the Eady growth rate anomalies in August and September
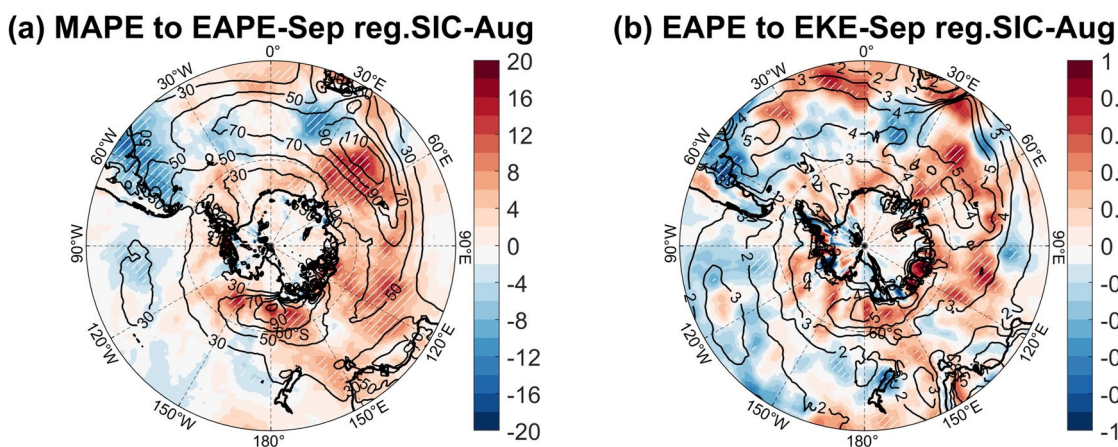

Fig. 14 Lagged regression of 850 hPa BCEC (W m^{-2}) from **a** MAPE to EAPE and **b** EAPE to EKE in September against the SIC time coefficients in August at lag 1 month. Hatching denotes regressions significant at the 95% confidence level

BCEC, as the BCEC is dynamically tied to the background state of the climate system (such as the topography, westerly jet, and ocean fronts). From the energetic perspective, the lost energy of the wave packets due to the barotropic decay and dissipation can be regained by the effective BCEC on the downstream side of the synoptic eddies which facilitates the downstream propagation without significant weakening (Orlanski and Chang 1993; Zhang et al. 2020).

Since storm track anomalies induced by the anomalous baroclinicity can extend downstream from its source region, another question remains as to the sea ice anomalies in which region is most effective in modulating the storm tracks. We choose the regionally averaged SIC indices in the ABS, the AP, and the Indian Ocean to represent the sea ice variability in those regions. The simultaneous regression

patterns of the SIC anomalies against the three indices suggests that the sea ice variabilities in the three regions are relatively independent. While the positive SIC anomalies in the ABS are weakly correlated with negative SIC anomalies in the Atlantic sector, the SIC near the AP and in the Indian Ocean does not show significant correlation with sea ice anomalies in other parts of Antarctica. The mutually independent nature justifies the use of these indices. As shown in Fig. 15, the storm track response to the SIC anomalies can be largely regarded as the linear combination of the effect of the sea ice anomalies in the three regions (cf. Fig. 11). The storm track anomalies induced by the SIC anomalies in the ABS and the AP cancels out over the central to eastern Pacific sector, while the SIC anomalies in the three regions all strengthen the storm track anomalies over the Indian
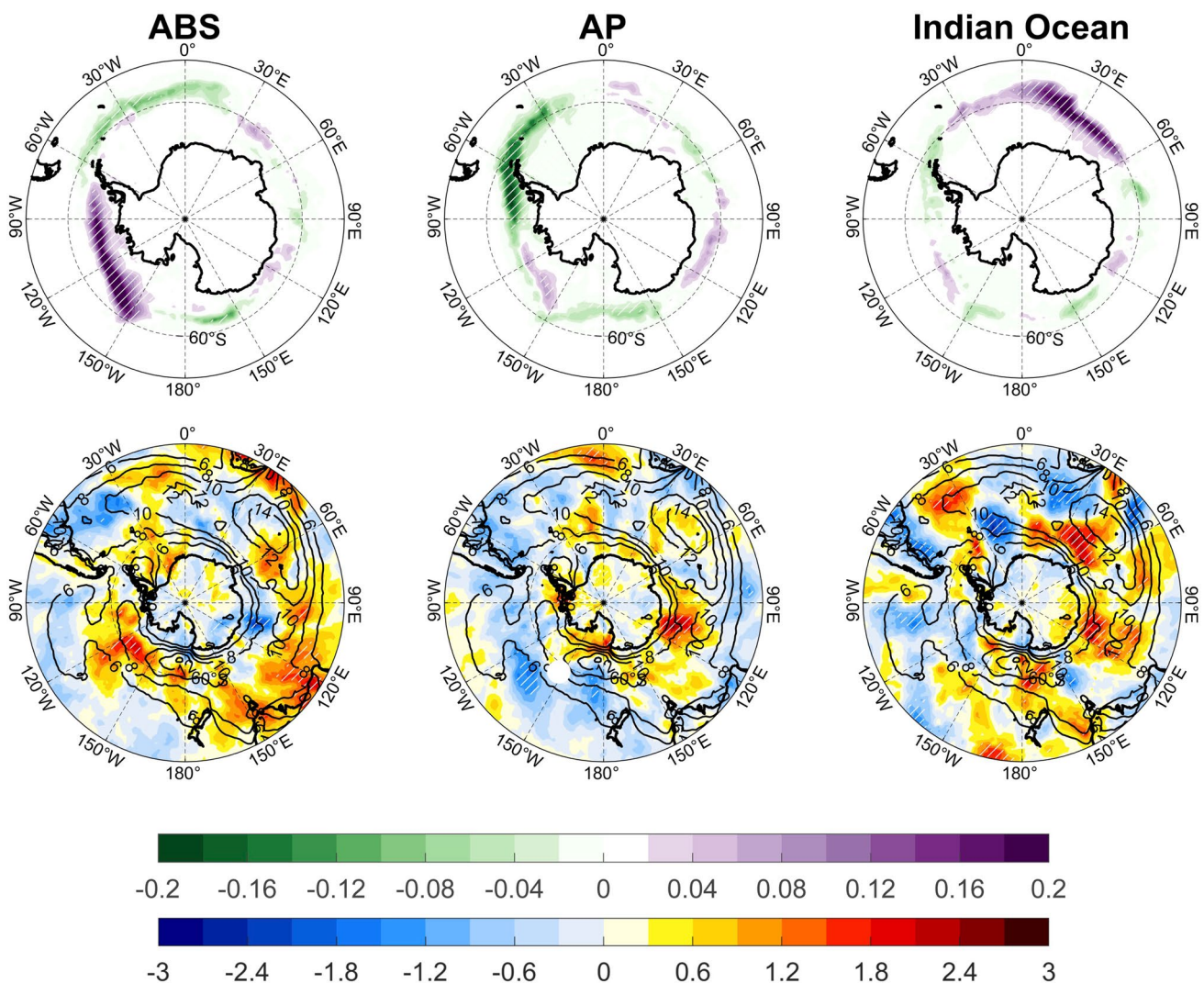

Fig. 15 Lagged partial regression of the midlatitude (top) SIC (%) in August and (bottom) 850 hPa $\langle v'T' \rangle$ in September against the normalized SIC time series in the Amundsen Sea, Peninsula and Indian Ocean in August, respectively (derived from the area-averaged SIC in the respective domain outlined in Fig. 11, with the signs of the regressions against the Antarctic Peninsula reversed to match the spatial distribution in Fig. 11). Hatching denotes regressions significant at the 95% confidence level

Ocean sector. The overall effect of the sea ice anomalies on the storm enhances the storm activities in the mid-latitude Indian Ocean. A closer examination reveals that the SIC anomalies in ABS and central Indian Ocean have relatively larger contribution to the storm track activities than the SIC anomalies in the AP, consistent with the larger net heat flux anomalies (recall Fig. 12). This indicates that these two regions are important baroclinic sources for synoptic eddy development.

5　Summary with discussion

The present study investigates the two-way interactions between the SH storm tracks and the sea ice anomalies in the Antarctic region. Using the lagged MCA methods, we have identified that the storm track activities have a prolonged impact on the Antarctic SIC in austral winter. The anomalously positive storm track activities in June and July are associated with a zonal SIC dipole with positive SIC anomalies in the ABS and negative SIC anomalies over the AP regions and seasonally varied SIC anomalies in the eastern Hemisphere. Despite the distinct distribution of the storm track anomalies in the June and July, we have shown that they can modulate the large-scale atmospheric circulations in a similar fashion. The associated low-level wind anomalies then influence the sea ice by both direct mechanical forcing and thermal forcing. Specifically for the thermal forcing, the meridional wind anomalies induce anomalous meridional heat transport which act to modulate SAT, while in some regions, the anomalous longwave radiation induced by the water vapor anomalies also contributes. The SIC anomalies can last for several months due to the persistent nature of the sea ice.

SIC anomalies can feed back to the storm track activities, which is most prominent for the SIC in August. The leading mode of the SIC anomalies bears much resemblance to one forced by the storm track activities in early months, suggesting a two-way interaction between the Antarctic sea ice and the SH storm track. The SIC anomalies reflects the spatial migration of the sea ice edges. Specifically, the sea ice extends equatorward if the SIC anomalies are positive, which consequently enhances (suppresses) the atmospheric baroclinicity on the equatorward (poleward) flank of the SIC anomaly centers. By diagnosing the Eady growth rate and baroclinic energy conversion, we have found that the SIC anomalies obtained by the first MCA mode can intensifies the storm track activities in the midlatitude Indian Ocean.

The two-way interactions between sea ice and storm tracks identified in this paper is most significant during the cold season, consistent with the seasonally asymmetric response of the storm tracks to the perturbed sea ice experiments (Kidston et al. 2011). This is because the sea ice edges, accompanied by the modulated atmospheric baroclinicity, extends to lower latitude in austral winter, making the storm track more susceptible to the sea ice variability. On the other hand, the sea ice shows strongest interannual variability during winter (e.g. Eayrs et al. 2019) and that is probably why the two-way interactions are most prominent in that season. Apart from transient eddy flux anomalies discussed in the main text, the SIC anomalies can also influence the midlatitude atmosphere by anomalous diabatic heating, which involves complex eddy-mean flow interactions (Fang and Yang 2016; Gu et al. 2018). In addition, the feedback of sea ice variability to the atmosphere varies among different regions with different amplitudes (England et al. 2018). Therefore, the quantitative relationship between the Antarctic sea ice and midlatitude atmosphere are still uncertain, and requires further examination.

The MCA has been widely used in the studies seeking for the climatic imprints (e.g., Frankignoul and Kestenare 2005; Liu et al. 2006; Gan and Wu 2013, 2015; Zhang et al. 2018, 2020). It should be noted that the detected lead or lag relationship between the storm track and sea ice primarily reflects the persistence or inertia of the SIC anomalies rather than the occurrence of the storm track of sea ice forcing in advance (right panel in Fig. 2), as pointed out by Czaja and Frankignoul (2002). According to the autocorrelations of $\langle v'T' \rangle$ and SIC (Fig. S6), the SIC anomalies in July and August can last for up to 4 months, while the storm track anomalies quickly drop to near zero in just 1-month lead or lag in austral winter. Indeed, similar anomalous sec ice and storm tracks can also be found in simultaneous heterogeneous maps (not shown).

It is well known that, variability in the circulation of the Amundsen Sea Low (ASL) (Raphael and Hobbs 2014; Raphael et al. 2016)—inked to internal tropical ocean variability and subsequent tropical–polar teleconnections (e.g. Schneider et al. 2012a, b)—has been found to be important. Combined with internal variability (Renwick et al. 2012; Clem et al. 2016), driven in particular by the SAM, these anomalous circulation features impact sea ice distribution. The associated SAT, wind, and precipitation anomalies then forces the Antarctic sea ice through dynamic and thermodynamic processes. Recent studies show that the storm track activities play a key role in modulating the tropical-polar teleconnections. Specifically, the storm tracks can modulate the tropic-polar teleconnection originated from both tropical Indian Ocean (McIntosh and Hendon 2018) and tropical Pacific (Guo et al. 2022). The present paper highlights the storm track as an independent source that drives SIC anomalies. The diagnostics with the geopotential tendency equation suggests that the storm track anomalies in June and July are indeed the driver, rather than the results, of the large-scale atmospheric circulation anomalies. On the other hand, how the relationship between the mesoscale processes

(e.g., oceanic fronts and eddies) coupling with storm track activities and sea ice variability remains an open question. As low-resolution climate models are likely to underestimate the effect of mesoscale processes (e.g., oceanic fronts and eddies) on storm track activities, as well as subsequent climate effects (Chang et al. 2020), it is important to further investigate this issue using the high-resolution (e.g., eddy-resolving) climate models in the future.

Declarations

Conflict of interest The authors declare that there is no conflict of interest.

Ethical approval Not applicable.

References

Alexander MA, Bhatt US, Walsh JE, Timlin MS, Miller JS, Scott JD (2004) The atmospheric response to realistic Arctic sea ice anomalies in an AGCM during winter. J Clim 17:890–905

Arblaster JM, Meehl GA (2006) Contributions of external forcings to southern annular mode trends. J Clim 19:2896–2905

Blackmon ML, Wallace JM, Lau NC, Mullen SL (1977) An observational study of the Northern Hemisphere winter-time circulation. J Atmos Sci 34:1040–1053

Branstator G (1995) Organization of storm track anomalies by recurring low-frequency circulation anomalies. J Atmos Sci 52:207–226

Brayshaw D, Hoskins BJ, Blackburn MJ (2008) The storm track response to idealized SST perturbations in an aquaplanet GCM. J Atmos Sci 65:2842–2860

Cai M, Mak M (1990) Symbiotic relation between planetary and synoptic scale waves. J Atmos Sci 47:2953–2968

Cai M, Yang S, Van den Dool HM, Kousky VE (2007) Dynamical implications of the orientation of atmospheric eddies: a local energetics perspective. Tellus 59:127–140

Chang P et al (2020) An unprecedented set of high-resolution earth system simulations for understanding multiscale interactions in climate variability and change. J Adv Model Earth Syst 12:e2020MS002298

Ciasto LM, Simpkins GR, England MH (2015) Teleconnections between tropical Pacific SST anomalies and extratropical Southern Hemisphere climate. J Clim 28:56–65

Clem KR, Renwick JA, McGregor J, Fogt RL (2016) The relative influence of ENSO and SAM on Antarctic Peninsula climate. J Geophys Res Atmos 121:9324–9341

Czaja A, Frankignoul C (2002) Observed impact of Atlantic SST anomalies on the North Atlantic oscillation. J Clim 15:606–623

Eady ET (1949) Long waves and cyclone waves. Tellus 1:33–52

Eayrs C, Holland D, Francis D, Wagner T, Kumar R, Li X (2019) Understanding the seasonal cycle of Antarctic Sea ice extent in the context of longer-term variability. Rev Geophy 57:1037–1064

England M, Polvani LM, Sun L (2018) Contrasting the Antarctic and Arctic atmospheric responses to projected sea ice loss in the late twenty-first century. J Clim 31:6353–6370

Fang J, Yang XQ (2016) Structure and dynamics of decadal anomalies in the wintertime midlatitude North Pacific ocean–atmosphere system. Clim Dyn 47:1989–2007

Fraedrich K, Ludz M (1987) A modified time-longitude diagram applied to 500 mb height along 50 degrees north and south. Tellus 39:25–32

Francis D, Eayrs C, Cuesta J, Holland D (2019) Polar cyclones at the origin of the reoccurrence of the Maud Rise Polynya in austral winter 2017. J Geophys Res Atmos 124:5251–5267

Francis D, Mattingly KS, Temimi M, Massom R, Heil P (2020) On the crucial role of atmospheric rivers in the two major Weddell Polynya events in 1973 and 2017 in Antarctica. Sci Adv 6:eabc2695

Frankignoul C, Kestenare E (2005) Air–sea interactions in the tropical Atlantic: a view based on lagged rotated maximum covariance analysis. J Clim 18:3874–3890

Gan B, Wu L (2013) Seasonal and long-term coupling between wintertime storm tracks and sea surface temperature in the North Pacific. J Clim 26:6123–6136

Gan B, Wu L (2015) Feedbacks of sea surface temperature to wintertime storm tracks in the North Atlantic. J Clim 28:306–323

Gan B, Wang T, Wu L, Li J, Qiu B, Yang H, Zhang L (2022) A Mesoscale ocean-atmosphere coupled pathway for decadal variability of the Kuroshio Extension system Bolan Gan. J Clim 36:485–510

Gu S, Zhang Y, Wu Q, Yang XQ (2018) The linkage between arctic sea ice and midlatitude weather: in the perspective of energy. J Geophys Res Atmos 123:11536–11550

Guo Y, Wen Z, Zhu Y, Chen X (2022) Effect of the late-1990s change in tropical forcing on teleconnections to the Amundsen-Bellingshausen seas region during Austral Autumn. J Clim 35:1–36

Hobbs WR, Massom R, Stammerjohn S, Reid P, Williams G, Meier W (2016) A review of recent changes in Southern Ocean sea ice, their drivers and forcings. Glob Planet Change 143:228–250

Holland PR (2014) The seasonality of Antarctic sea ice trends. Geophys Res Lett 41:4230–4237

John T et al (2009) Non-annular atmospheric circulation change induced by stratospheric ozone depletion and its role in the recent increase of Antarctic sea ice extent. Geophys Res Lett 36:L08502

Kidston JA, Taschetto AS, Thompson DWJ, England M (2011) The influence of Southern Hemisphere sea-ice extent on the latitude of the mid-latitude jet stream. Geophys Res Lett 38:L15804

Kushnir Y, Robinson WA, Blade I, Hall NMJ, Peng S, Sutton R (2002) Atmospheric GCM response to extratropical SST anomalies: synthesis and evaluation. J Clim 15:2233–2256

Lecomte O, Goosse H, Fichefet T, Lavergne CD, Barthélemy A, Zunz V (2017) Vertical ocean heat redistribution sustaining sea-ice concentration trends in the Ross Sea. Nat Commun 8:258

Lee S, Held IM (1993) Baroclinic wave packets in models and observations. J Atmos Sci 50:1413–1428

Li X, Holland DM, Gerber EP, Yoo C (2014) Impacts of the north and tropical Atlantic Ocean on the Antarctic Peninsula and sea ice. Nature 505:538–542

Li X et al (2021) Tropical teleconnection impacts on Antarctic climate changes. Nat Rev Earth Environ 2:680–698

Li Y, Zhang L, Gan B, Wu L (2023) Observed contribution of Barents-Kara sea ice loss to winter Warm Arctic-Cold Eurasia anomaly. Environ Res Lett 18:034019

Liu Q, Wen N, Liu Z (2006) An observational study of the impact of the North Pacific SST on the atmosphere. Geophys Res Lett 33:L18611

Luo D, Diao Y, Feldstein SB (2011) The variability of the Atlantic storm track and the North Atlantic Oscillation: a link between intraseasonal and interannual variability. J Atmos Sci 68:577–601

McIntosh P, Hendon H (2018) Understanding Rossby wave trains forced by the Indian Ocean Dipole. Clim Dyn 50:2783–2798

Meehl GA, Arblaster JM, Bitz CM, Chung CT, Teng H (2016) Antarctic sea-ice expansion between 2000 and 2014 driven by tropical Pacific decadal climate variability. Nat Geosci 9:590–595

Meehl GA, Arblaster JM, Chung CT, Holland MM, DuVivier A, Thompson L, Yang D, Bitz CM (2019) Sustained ocean changes contributed to sudden Antarctic sea ice retreat in late 2016. Nat Commun 10:1–9

Menéndez CG, Serafini V, Le Treut H (1999) The effect of sea-ice on the transient atmospheric eddies of the Southern Hemisphere. Clim Dyn 15:659–671

Nakamura H, Shimpo A (2004) Seasonal variations in the Southern Hemisphere storm tracks and jet streams as revealed in a reanalysis data set. J Clim 17:1828–1842

Nakamura H, Sampe T, Goto A, Ohfuchi W, Xie SP (2008) On the importance of midlatitude oceanic frontal zones for the mean state and dominant variability in the tropospheric circulation. Geophys Res Lett 35:L15709

Nishii K, Nakamura H, Miyasaka T (2009) Modulations in the planetary wave field induced by upward-propagating Rossby wave packets prior to stratospheric sudden warming events: a case-study. Q J R Meteorol Soc 135:39–52

Ogawa F, Nakamura H, Nishii K, Miyasaka T, Kuwano-Yoshida A (2012) Dependence of the climatological axial latitudes of the tropospheric westerlies and storm tracks on the latitude of an extratropical oceanic front. Geophys Res Lett 39:L05804

Orlanski I, Chang EKM (1993) Ageostrophic geopotential fluxes in downstream and upstream development of baroclinic waves. J Atmos Sci 50:212–225

Overland J, Francis JA, Hall R, Hanna E, Kim SJ, Vihma T (2015) The melting Arctic and midlatitude weather patterns: are they connected? J Clim 28:7917–7932

Overland J et al (2016) Nonlinear response of mid-latitude weather to the changing Arctic. Nat Clim Change 6:992–999

Purich A, England MH (2019) Tropical teleconnections to Antarctic sea ice during austral spring 2016 in coupled pacemaker experiments. Geophys Res Lett 46:6848–6858

Raphael MN, Hobbs W (2014) The influence of the large-scale atmospheric circulation on Antarctic sea ice during ice advance and retreat seasons. Geophys Res Lett 41:5037–5045

Raphael MN, MaRshall GJ, Turner J, Fogt RL, Schneider D, Dixon DA, Hosking JS, Jones JM, Hobbs WR (2016) The Amundsen Sea low: variability, change, and impact on Antarctic climate. Bull Am Meteorol Soc 97:111–121

Ren X, Li Z, Cai W, Li X, Wang CY, Jin Y, Wu L (2022) Influence of tropical Atlantic meridional dipole of sea surface temperature anomalies on Antarctic autumn sea ice. Environ Res Lett 17:094046

Renwick JA, Kohout A, Sam D (2012) Atmospheric forcing of Antarctic sea ice on intraseasonal time scales. J Clim 25:5962–5975

Sato K, Simmonds I (2021) Antarctic skin temperature warming related to enhanced downward longwave radiation associated with increased atmospheric advection of moisture and temperature. Environ Res Lett 16:064059

Schemm S (2018) Regional trends in weather systems help explain Antarctic sea ice trends. Geophys Res Lett 45:7165–7175

Schneider DP, Deser C, Okumura Y (2012a) An assessment and interpretation of the observed warming of West Antarctica in the austral spring. Clim Dyn 38:323–347

Schneider DP, Okumura Y, Deser C (2012b) Observed Antarctic interannual climate variability and tropical linkages. J Clim 25:4048–4066

Sen Gupta A, England MH (2007) Coupled ocean, atmosphere feedback in the Southern Annular Mode. J Clim 20:3677–3692

Simmonds I, Budd WF (1991) Sensitivity of the Southern Hemisphere circulation to leads in the Antarctic pack ice. Q J R Meteorol Soc 117:1003–1024

Simmonds I, Wu X (1993) Cyclone behaviour response to changes in winter Southern Hemisphere sea-ice concentration. Q J R Meteorol Soc 119:1121–1148

Thompson DWJ, Solomon S (2002) Interpretation of recent Southern Hemisphere climate change. Science 296:895–899

Trenberth KE (1986) An assessment of the impact of transient eddies on the zonal flow during a blocking episode using localized Eliassen–Palm flux diagnosis. J Atmos Sci 43:2070–2087

Trenberth KE, Caron JM (2001) Estimates of meridional atmosphere and ocean heat transports. J Clim 14:3433–3443

Trenberth KE, Stepaniak DP (2003) Covariability of components of poleward atmospheric energy transports on seasonal and interannual timescales. J Clim 16:3691–3705

Tsukernik M, Lynch AH (2013) Atmospheric meridional moisture flux over the Southern Ocean: a story of the Amundsen Sea. J Clim 26:8055–8064

Wu Q, Zhang X (2011) Observed evidence of an impact of the Antarctic sea ice dipole on the Antarctic oscillation. J Clim 24:4508–4518

Yuan X (2004) ENSO-related impacts on Antarctic sea ice: a synthesis of phenomenon and mechanisms. Antarctic Sci 16:415–425

Zhang L, Gan B, Wu L, Cai W, Ma H (2018) Seasonal dependence of coupling between storm tracks and sea surface temperature in

the Southern Hemisphere midlatitudes: a statistical assessment. J Clim 31:4055–4074

Zhang L, Delworth TL, Cooke W, Yang X (2019) Natural variability of Southern Ocean convection as a driver of observed climate trends. Nat Clim Change 9:59–65

Zhang L, Gan B, Wang H, Wu L, Cai W (2020) Essential role of the midlatitude South Atlantic variability in altering the Southern Hemisphere summer storm tracks. Geophys Res Lett 47:e2020GL087910

Zhang L, Gan B, Li X, Wang H, Wang C, Cai W, Wu L (2021) Remote influence of the midlatitude South Atlantic variability in spring on Antarctic summer sea ice. Geophys Res Lett 48:e2020GL090810